

Lithium-rich field giants in the Sloan Digital Sky Survey

S. L. Martell^{1*} and M. D. Shetrone²

¹*Australian Astronomical Observatory, North Ryde NSW 2122, Australia*

²*McDonald Observatory, University of Texas Austin, McDonald Observatory, Texas 79734, USA*

Received 25 October 2012/ Accepted 19 December 2012

ABSTRACT

We present a search for post-main-sequence field stars in the Galaxy with atypically large lithium abundances. Using moderate-resolution spectra taken as part of the Sloan Digital Sky Survey, along with high-resolution followup spectroscopy from the Hobby-Eberly Telescope, we identify 23 post-turnoff stars with $\log\epsilon(\text{Li})$ greater than 1.95, including 14 with $\log\epsilon(\text{Li}) \geq 2.3$ and 8 with $\log\epsilon(\text{Li}) \geq 3.0$, well above the low level expected for evolved stars. Comparison with theoretical isochrones indicates that some of our Li-rich stars are affiliated with the upper red giant branch, the asymptotic giant branch and the red clump rather than the RGB bump, which is a challenge to existing models of Li production in evolved stars.

Key words: Stars: abundances

1 INTRODUCTION

The abundance of lithium is extremely sensitive to the ambient conditions inside stars, since its cross section to proton capture is quite large at temperatures above $2.6 \times 10^6 \text{ K}$. Li is readily destroyed in the interiors of low-mass main-sequence stars, and the Li in the convective envelope is progressively depleted as envelope material is cycled past the innermost, hottest region of the convective zone. Surface Li abundance is further depleted after stars leave the main sequence and undergo first dredge-up (Iben 1968), in which the convective envelope deepens, mixing fusion-processed material from the stellar interior into the envelope and exposing envelope material to even higher temperatures.

Because of this, it was quite surprising when Wallerstein & Sneden (1982) discovered a Li-rich K giant serendipitously while investigating barium-rich field stars. More systematic searches for Li-rich stars (e.g., Brown et al. 1989; Pilachowski 1986; Pilachowski et al. 1988; Pilachowski et al. 2000) found that they are rare in the Solar neighborhood and extremely unusual in globular clusters. The study of Charbonnel & Balachandran (2000) found that nearby Solar-metallicity Li-rich stars are either low-mass stars ($M \simeq 1M_{\odot}$) near the “bump” in the red giant branch (RGB) luminosity function or intermediate-mass stars ($M \simeq 3M_{\odot}$) low on the asymptotic giant branch (AGB). In both cases, the hydrogen-burning shell in the stars in question has recently encountered, and destroyed, the discontinuity in mean molecular weight (the “ μ -barrier”) left behind at the end of first dredge-up. In low-mass red giants, the destruction of the μ -barrier causes a brief loop in stellar evolution, observed as the RGB bump, and permits deep mixing, a nonconvective process that steadily cycles material between the photosphere and the radiative zone, causing surface abundances of

carbon and nitrogen to evolve constantly as stars ascend the RGB (see Martell et al. 2008 for a more thorough explanation of deep mixing). In higher-mass stars, the destruction of the μ -barrier occurs at **second** dredge-up, low on the asymptotic giant branch. The fact that the Li-rich stars identified by Charbonnel & Balachandran (2000) were located near the destruction of the μ -barrier led those authors to speculate that the onset of deep mixing produces a brief episode of Li production via the Cameron-Fowler mechanism (Cameron & Fowler 1971). In this process, ^7Be produced by the proton-proton chain is transported to a cooler zone in the star, where it captures an electron and decays into ^7Li , which is stable against proton capture if its surroundings are cool enough. A phase in which the deep-mixing mass transport speed was briefly high enough to allow this process would cause surface Li abundances to rise sharply and then decay.

However, the existence of Li-rich stars in other regions of the Hertzsprung-Russell diagram challenges this model: Kraft et al. (1999) found one bright red giant well above the RGB bump in the globular cluster M3, where deep mixing is well known to operate (Smith 2002; Angelou et al. 2011). More recently, six independent studies in the past three years have reported a total of 47 new Li-rich post-main-sequence stars. These new Li-rich stars fill a broad range of parameter space: low-mass ($M \leq 2M_{\odot}$) RGB stars in the thick disk with $-1 \leq [\text{Fe}/\text{H}] \leq 0$ (Monaco et al. 2011); an intermediate-mass ($M \simeq 4M_{\odot}$), Solar-metallicity star in the thin disk (Monaco et al. 2011); low-mass RGB stars with $[\text{Fe}/\text{H}] \simeq -0.9$ in the Galactic bulge (Gonzalez et al. 2009; Lebzelter et al. 2012); and low-mass RGB stars in Local Group dwarf galaxies, two of which have $[\text{Fe}/\text{H}] \simeq -2.7$ (Kirby et al. 2012).

Two of the recent studies (Kumar et al. 2011 and Ruchti et al. 2011) take the approach of selecting a well-defined subset from an existing catalog (*Hipparcos* and RAVE, respectively) for high-resolution spectroscopic followup and abundance analysis, a procedure that we also adopt. In this paper, we present a search for Li-

* Email: smartell@aao.gov.au (SLM); shetrone@as.utexas.edu (MDS)

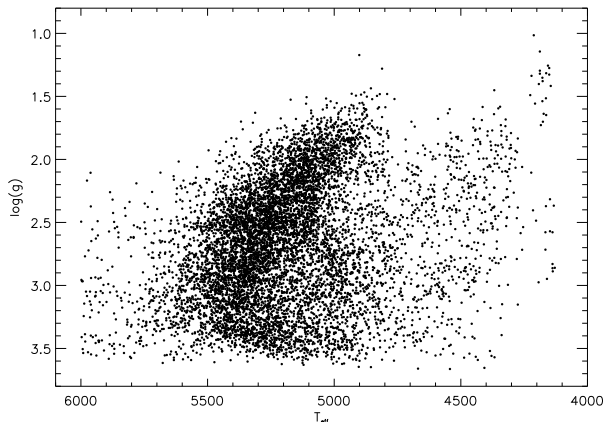


Figure 1. Distribution of T_{eff} and $\log(g)$ for the 8535 stars in our initial data set.

rich field stars in Sloan Digital Sky Survey (SDSS) spectroscopy. By surveying stars across a wide range of metallicity and surface gravity, we are able to take a broad view of the question of Li-rich post-main-sequence stars. This paper describes the 23 previously unknown Li-rich stars we identified from this original data set, and explores whether the various proposed mechanisms for Li production in evolved stars are sufficient to explain this group of Li-rich stars.

2 THE OBSERVATIONAL DATA SET

In order to explore the physical conditions that produce large amounts of photospheric lithium in some evolved stars, we selected a sample of post-main-sequence stars from the SDSS Data Release 7. The 8535 stars in our initial data set were required to have high-quality spectra and relatively low errors on stellar parameters determined by the automated SSPP pipeline (Lee et al. 2008a), and were allowed to cover a broad range of metallicity, effective temperature and surface gravity.

2.1 SDSS spectroscopy

The imaging component of the original Sloan Digital Sky Survey and its extensions (Fukugita et al. 1996; Gunn et al. 1998; York et al. 2000; Pier et al. 2003; Gunn et al. 2006; Stoughton et al. 2002; Abazajian et al. 2003, 2004, 2005; Adelman-McCarthy et al. 2006, 2007, 2008; Abazajian et al. 2009; Aihara et al. 2011) includes *ugriz* photometry for several hundred million stars. SEGUE (Yanny et al. 2009), one of three sub-surveys that together formed SDSS-II, extended that imaging footprint by approximately 3500 deg², and also obtained $R \simeq 2000$ spectroscopy for approximately 240,000 stars over a wavelength range of 3800 – 9200Å. Additional spectroscopy with similar characteristics has been taken as part of the SDSS Legacy project (Abazajian et al. 2009) and in preparation for the SDSS-III Multi-object APO Radial Velocity Exoplanet Large-area Survey (MARVELS) project (Ge et al. 2008). To facilitate the development and calibration of the SEGUE Stellar Parameter Pipeline (SSPP; Lee et al. 2008a; Lee et al. 2008b; Allende Prieto et al. 2008), SEGUE included spectra for a collection of Galactic globular and open clusters. As described in Lee et al. (2008a), SSPP produces estimates of T_{eff} , $\log(g)$,

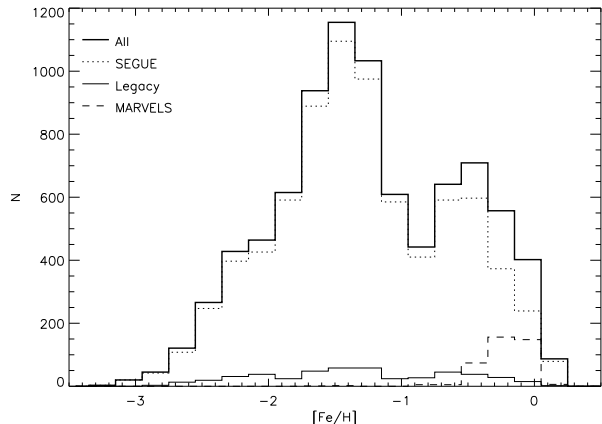


Figure 2. Metallicity histogram for our initial data set (heavy solid line), with histograms for the three data sources overplotted with a dotted line (SEGUE), light solid line (Legacy) and dashed line (MARVELS).

$[\text{Fe}/\text{H}]$, and radial velocity, along with the equivalent widths and/or line indices for 85 atomic and molecular absorption lines, by processing the calibrated spectra generated by the standard SDSS spectroscopic reduction pipeline (Stoughton et al. 2002). Additional validations and details of recent updates to SSPP are discussed in Smolinski et al. (2011).

2.2 Target selection

We selected our sample from the seventh SDSS data release (DR7), using the online Catalog Archive Server (CAS)¹ to identify stars with a mean signal-to-noise ratio per pixel (SNR) of at least 40, $T_{\text{eff}} \leq 6000\text{K}$, reasonable errors on $[\text{Fe}/\text{H}]$ metallicity ($\sigma_{[\text{Fe}/\text{H}]} \leq 0.3$) and surface gravity ($\sigma_{\log(g)} \leq 0.5$), and surface gravity no higher than 1.4 dex greater than the surface gravity at the “bump” in the RGB luminosity function. Previous studies have found that stars with unexpectedly high lithium abundances tend to be near the RGB bump, so we designed this gravity selection to include stars at evolutionary phases from shortly before the RGB bump to the tip of the RGB. Empirically, the luminosity of the RGB bump is a function of metallicity: Fusi Pecci et al. (1990) report $[\text{Fe}/\text{H}]$ versus M_V^{bump} for a selection of Galactic globular clusters, and we converted those M_V values to $\log(g)$ using metallicity-matched 12 Gyr Yale-Yonsei isochrones (Demarque et al. 2004), then fit a least-squares line to derive $\log(g)_{\text{bump}} = 2.23235 + (0.188018 \times [\text{Fe}/\text{H}])$. This initial data set contained 8535 stars: 7667 from SEGUE, 471 from Legacy and 397 from MARVELS. Figure 1 shows T_{eff} versus $\log(g)$ for all 8535 stars, and Figure 2 is a histogram of the metallicities. In Figure 2, the heavy solid histogram shows the metallicity distribution for the full data set, with the histogram for just the SEGUE stars shown as a dotted line, the histogram for the Legacy stars drawn with a light solid line, and the histogram for the MARVELS stars shown with a dashed line.

3 LOW-RESOLUTION ANALYSIS

In order to identify stars with potentially high lithium abundance based on low-resolution spectra, we designed a spectral index,

¹ <http://skyservice.pha.jhu.edu/CasJobs/login.aspx>

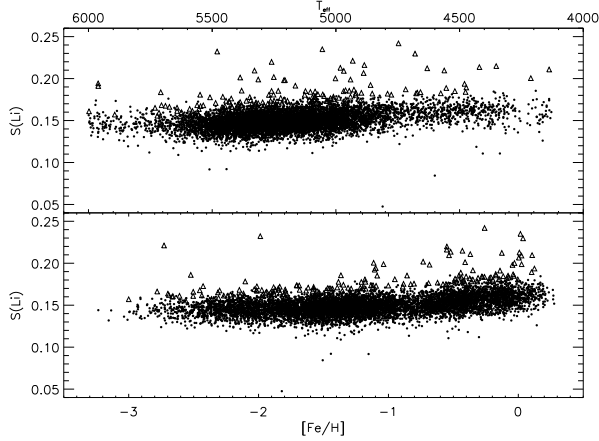


Figure 3. Lithium index $S(Li)$ versus T_{eff} for the initial data set (upper panel); $S(Li)$ versus $[Fe/H]$ (lower panel). In both panels, stars selected for the secondary data set are shown as open triangles.

$S(Li)$, that measures the magnitude difference between the integrated flux in the 6708Å resonance line and the integrated flux in a small region of nearby spectrum. It is defined as

$$S(Li) = -2.5 \times \log \frac{\int_{6706}^{6713} I_{\lambda} d\lambda}{\int_{6730}^{6738} I_{\lambda} d\lambda}.$$

Typically spectral indices are defined for use in small regions of parameter space, and use one or more nearby region(s) of spectrum independent of the property that drives variations in the feature of interest as a comparison band; however, our initial data set contains stars across such a wide range of T_{eff} , $\log(g)$ and $[Fe/H]$ that there are no nearby regions of spectrum that are the same for all of our stars. This fact introduces some scatter to our $S(Li)$ measurements, requiring extra care in selecting likely Li-enhanced stars for followup observations.

The upper panel of Figure 3 shows $S(Li)$ versus T_{eff} for the initial data set, and the lower panel shows $S(Li)$ versus $[Fe/H]$ for the same stars. In each plane, $S(Li)$ has a broad distribution at a fixed value of the independent parameter (T_{eff} or $[Fe/H]$) and a slight dependence on that parameter. To identify outliers in the $S(Li)$ - T_{eff} and $S(Li)$ - $[Fe/H]$ distributions, we select all stars with $S(Li) \geq 0.295 - \frac{T_{\text{eff}}}{4 \times 10^4}$ and $S(Li) \geq 0.18 + \frac{[Fe/H]}{100}$ as our secondary data set. There are 162 stars meeting both criteria, and these are plotted as open triangles in Figure 3, while all other stars from the initial data set are represented by small filled circles.

From by-eye examination each of the spectra in this secondary data set of 162 stars, we found that our selection criteria were generous: fewer than half of the stars selected based on $S(Li)$ - T_{eff} - $[Fe/H]$ position had 6708Å Li lines that appeared legitimately strong in the SDSS spectra. Figure 4 shows spectra for two of the stars we selected for high-resolution followup (the lower two spectra), as well as one star with little apparent absorption in the 6708Å Li line (top spectrum). We generated low-resolution synthetic spectra based on SSPP stellar parameters to roughly estimate lithium abundance for those potentially lithium-enhanced stars, and selected 36 of them for high-resolution followup observations, with the goal of determining more precise stellar parameters and $\epsilon(Li)$ abundances. Table 1 lists SDSS ID number, data source (SEGUE, Legacy or MARVELS), plug-plate number, modified Julian date of observation, fiber ID number, right ascension, declination, g mag-

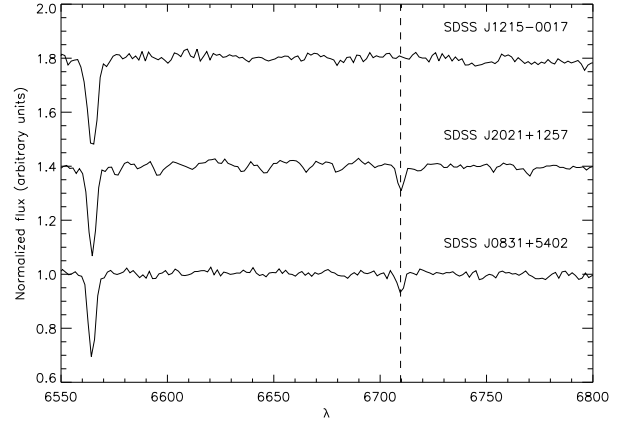


Figure 4. Typical spectra from our initial SDSS low-resolution data set. The lower two spectra appear to have strong absorption in the 6708Å Li resonance line, while the top spectrum does not.

nitude (V magnitude for the MARVELS stars) and $S(Li)$ measurement for the 36 stars initially flagged for followup spectroscopy. MARVELS stars are too bright to be included in SEGUE photometry, so their apparent V magnitudes were taken from the Vizier catalog-search service². The plate, MJD and fiberID information is given because it is a simple way for finding individual stars in the CAS.

4 HIGH-RESOLUTION ANALYSIS

Followup spectra were obtained for 34 of these 36 stars using the High-Resolution Spectrograph (HRS) on the Hobby-Eberly Telescope (HET) at McDonald Observatory (Tull 1998). All but one of these 34 stars were first observed as filler time (P4) during normal queue observing (Shetrone et al. 2007) during periods 2010T2 and 2011T1. This filler time allowed us to take an initial short snapshot spectrum to confirm the strength of the Li line; 7 were found to not be Li rich and 27 were confirmed Li rich. For 23 of these Li rich stars we were able to follow-up with additional spectra to get the SNR sufficient for determination of stellar parameters and abundances. One of the 36 stars (SDSS J0831+5402) had already been observed as part of the Chemical Abundances of Stars in the Halo (CASH) project (Frebel et al. 2008).

4.1 Spectroscopic Observations and Reduction

HRS was configured to HRS_15k_central_316g5936_2as_0sky_IS0_GC0_2x5 during our HET observations to achieve $R=18,000$ spectra covering 4233Å to 5900Å on the blue chip and 6000Å to 7850Å on the red chip. Exposure times per visit ranged from 300 seconds to 1800 seconds based on the observing conditions. Because of the nature of the HET and the generally poor conditions of filler time, some targets had multiple visits taken over a number of days to build up enough S/N to cleanly detect the Li feature.

The spectra were reduced with IRAF³ ECHELLE scripts.

² <http://vizier.cfa.harvard.edu/viz-bin/VizieR>

³ IRAF (Image Reduction and Analysis Facility) is distributed by the National Optical Astronomy Observatories, which are operated by the Associ-

Table 1. Star identifiers, position, photometry and lithium index for the 36 stars selected for followup spectroscopy. Apparent V magnitudes are listed for MARVELS stars.

SDSS ID	Source	Plate	MJD	FiberID	α	δ	g_0	$S(Li)$
Confirmed Li-rich with HET								
SDSS J2206+4531	SEGUE	2556	54000	640	22:06:19.75	45:31:57.19	15.732	0.209
SDSS J2353+5728	SEGUE	2377	53991	337	23:53:29.76	57:28:18.41	12.960	0.209
SDSS J0808-0815	SEGUE	2806	54425	256	08:08:34.33	-08:15:47.30	14.598	0.198
SDSS J0301+7159	MARVELS	2843	54453	634	03:01:33.77	71:59:11.16	10.570	0.197
SDSS J2019+6012	SEGUE	2554	54263	600	20:19:32.44	60:12:46.32	15.270	0.212
SDSS J0652+4052	MARVELS	2847	54452	557	06:52:37.80	40:52:01.44	11.170	0.212
SDSS J0245+7102	MARVELS	2843	54453	168	02:45:20.83	71:02:02.63	11.760	0.184
SDSS J0632+2604	SEGUE	2678	54173	188	06:32:30.90	26:04:37.46	15.152	0.234
SDSS J2356+5633	SEGUE	2377	53991	200	23:56:52.22	56:33:38.83	13.080	0.210
SDSS J0535+0514	MARVELS	2841	54451	299	05:35:43.75	05:14:22.62	12.310	0.191
SDSS J2200+4559	SEGUE	2556	54000	540	22:00:51.22	45:59:40.33	15.453	0.229
SDSS J0304+3823	SEGUE	2441	54065	453	03:04:37.40	38:23:46.12	15.357	0.181
SDSS J1901+3808	SEGUE	2536	53883	306	19:01:49.00	38:08:51.00	14.29	0.214
SDSS J0720+3036	SEGUE	2677	54180	255	07:20:42.79	30:36:51.49	16.667	0.209
SDSS J1909+3837	SEGUE	2536	53883	110	19:09:29.25	38:37:46.23	15.764	0.214
SDSS J1105+2850	SEGUE	2870	54534	599	11:05:36.91	28:50:08.09	17.006	0.185
SDSS J0654+4200	MARVELS	2847	54552	614	06:54:58.00	42:00:27.00	12.51	0.220
SDSS J1607+0447	SEGUE	2178	54629	378	16:07:09.23	04:47:12.73	16.139	0.173
SDSS J1310-0012	SEGUE	2901	54652	191	13:10:37.22	-00:12:44.40	15.252	0.185
SDSS J0936+2935	SEGUE	2889	54530	164	09:36:27.44	29:35:35.80	16.240	0.185
SDSS J1522+0655	SEGUE	2902	54629	33	15:22:11.86	06:55:55.22	15.912	0.165
SDSS J0831+5402	SEGUE	2316	53757	395	08:31:55.28	54:02:45.55	15.430	0.186
SDSS J1432+0814	SEGUE	2933	54617	107	14:32:07.15	08:14:06.15	17.047	0.221
Confirmed Li-rich with HET but not enough SNR for full analysis								
SDSS J0515+1558	SEGUE	2668	54084	214	05:15:23.17	15:58:55.38	14.555	0.216
SDSS J2048+5603	SEGUE	2555	54265	58	20:48:46.82	56:03:53.65	13.423	0.200
SDSS J2119-0734	SEGUE	2305	54414	230	21:19:47.65	-07:34:26.89	14.526	0.167
SDSS J1214+5027	SEGUE	2919	54537	630	12:14:54.88	50:27:00.99	18.205	0.177
Confirmed not Li-rich with HET								
SDSS J1421+0136	Legacy	534	51997	162	14:21:28.26	01:36:28.35	17.077	0.200
SDSS J1213-0147	Legacy	333	52313	331	12:13:53.32	-01:47:14.93	16.558	0.180
SDSS J1227-0026	SEGUE	2558	54140	115	12:27:12.72	-00:26:58.81	16.990	0.177
SDSS J0144-1005	SEGUE	2850	54461	12	01:44:49.17	-10:05:31.09	16.738	0.171
SDSS J0352-0540	SEGUE	2051	53738	357	03:52:43.59	-05:40:03.32	16.487	0.168
SDSS J1725+0729	SEGUE	2797	54616	304	17:25:04.06	07:29:45.03	14.807	0.168
SDSS J1849+1931	SEGUE	2812	54633	393	18:49:52.58	19:31:04.20	14.980	0.168
Not observed with HET								
SDSS J1824+7911	SEGUE	2802	54326	372	18:24:22.51	79:11:24.47	16.548	0.201
SDSS J2021+1257	SEGUE	2248	53558	291	20:21:25.73	12:57:51.33	15.263	0.198

The standard IRAF scripts for overscan removal, bias subtraction, flat fielding and scattered light removal were employed. For the HRS flat field we masked out the Li I and Na D regions because the HET HRS flat field lamp suffered from intermittent faint emission lines which would otherwise compromise our analysis. Equivalent widths (EW) were measured using the IRAF task *splot* and forcing the Gaussian fit to have fixed FWHM for those lines below 150 mÅ while allowing the strong lines to have a variable FWHM. We also fit multiple Gaussian profiles to any nearby lines to take blends into account. Metallicity and α -element abundances were determined through equivalent width analysis; oscillator strengths adopted for the EW analysis were taken from Fulbright et al. (2006), Fulbright et al. (2007),

Johnson & Pilachowski (2010), and Koch & McWilliam (2008). Lithium abundance was determined by spectral synthesis of the 6708Å and 6104Å resonance lines. We also determined carbon abundance and $^{12}\text{C}/^{13}\text{C}$ ratios, where possible, by synthesis of the 4297Å CH feature. The CH linelist for the carbon analysis was taken from Plez (priv. comm.); all other lines were taken from a version of the Kurucz & Bell (1995) linelist modified to fit the strongest lines to the Solar spectrum. Model atmospheres were taken from the Osmares 2005 grid (Gustafsson et al. 2008), interpolating between the grid points. These spherical models cover metallicity ranges from +1.0 to -3.0 with $[\alpha/\text{Fe}] = +0.4$ for $[\text{Fe}/\text{H}] < -1.5$, $[\alpha/\text{Fe}] = +0.3$ for $[\text{Fe}/\text{H}] = -0.75$, $[\alpha/\text{Fe}] = +0.2$ for $[\text{Fe}/\text{H}] = -0.5$, $[\alpha/\text{Fe}] = +0.1$ for $[\text{Fe}/\text{H}] = -0.25$ and $[\alpha/\text{Fe}] = +0.$ for $[\text{Fe}/\text{H}] \geq 0.0$.

The abundance calculations were performed using a modified version of the 2010 version of the LTE line analysis and spectrum synthesis code MOOG (Snedden 1973). This code has some sig-

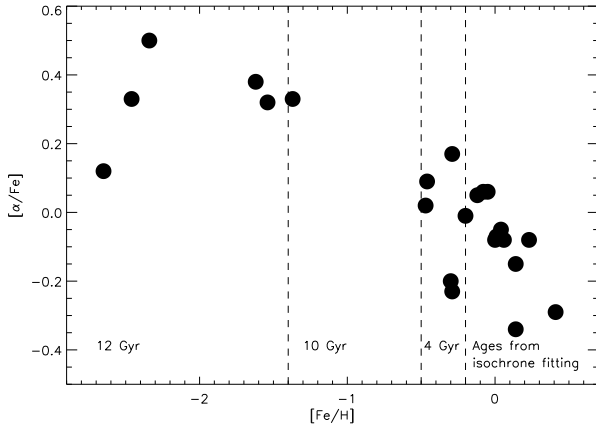


Figure 5. The 23 stars for which we derive high-resolution stellar parameters and abundances, in the $\alpha - \text{Fe}$ plane. Dashed lines mark the borders of our rough age estimations.

nificant differences from the earlier versions including using the predicted abundance vs. reduced EW for determining the microturbulence. Initial estimates of the stellar parameters were taken from the SSPP pipeline. From this starting point the temperature was adjusted until there was no significant slope in the Fe I abundances with respect to line excitation potential. The stellar gravity was adjusted such that the Fe I and Fe II lines produced the same abundance within the errors. Microturbulence was determined by requiring that there was no significant slope in the Fe I abundance vs. predicted Fe I reduced equivalent widths based on the mean abundance of the lines.

Table 2 lists SDSS ID, along with T_{eff} , $\log(g)$ and $[\text{Fe}/\text{H}]$ and their associated errors, plus microturbulent velocity and rotational velocity, where measurable, derived from our high-resolution spectra, and Table 3 lists SDSS ID and abundances of $[\alpha/\text{Fe}]$, $[\text{C}/\text{Fe}]$, $^{12}\text{C}/^{13}\text{C}$, and $\log\epsilon(\text{Li})$ determined from synthesis of the 6707Å and 6104Å lines. Alpha-element abundances are the error-weighted average of $[\text{Mg}/\text{Fe}]$, $[\text{Ca}/\text{Fe}]$ and $[\text{Ti}/\text{Fe}]$, and the total error on $[\alpha/\text{Fe}]$ is the larger of the propagated errors or the dispersion in the three input abundances.

4.2 Evolutionary states of the stars

Previous searches for Li-rich stars have focused on groups of stars with similarities: for example, Lebzelter et al. (2012) selected only RGB stars in the Galactic bulge, with metallicities in a narrow range, and Kumar et al. (2011) use the *Hipparcos* catalog, in which the distances to all stars are known quite precisely, as their initial data set. However, our data set is heterogeneous in terms of age, composition and position in the Galaxy. Based on the metallicities and alpha-enhancements derived from the high-resolution spectra, we divide our Li-rich stars into four broad groups and assign representative ages. Figure 5 shows the four groups in the $[\alpha/\text{Fe}] - [\text{Fe}/\text{H}]$ plane, which is commonly used to compare the star-formation and chemical-enrichment histories of composite stellar populations in dwarf galaxies to the components of the Milky Way (e.g., Venn et al. 2003; Shetrone et al. 2003; Koch et al. 2008; Kirby et al. 2011). Briefly, moderate- and low-metallicity stars are assumed to be old, while higher-metallicity, non- α -enhanced stars are significantly younger. For the highest-metallicity stars in the sample ($[\text{Fe}/\text{H}] \geq -0.2$), we use isochrones to estimate the ages.

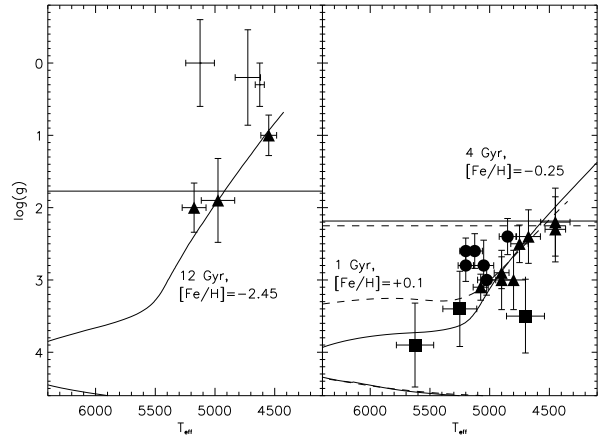


Figure 6. Effective temperature and surface gravity from high-resolution analysis, with measurement errors, for our 23 Li-rich stars. Lower-metallicity stars are in the left panel, and higher-metallicity stars are in the right panel. The different symbols represent groups in evolutionary phase, and representative isochrones are overplotted. Horizontal lines mark the position of the RGB bump on each isochrone, as calculated from our empirical relation given in Section 2.2. Triangles are RGB stars, circles are red clump stars, and squares are stars that have not yet reached first dredge-up (whose Li abundances are not relevant to the question of Li production on the RGB). The three plain crosses at the top of the left panel are stars whose $\log(g)$ and T_{eff} are not compatible with any reasonable isochrone, and we believe them to be post-AGB stars.

Figure 6 demonstrates that our initial $[\alpha/\text{Fe}] - [\text{Fe}/\text{H}]$ age estimation was reasonable: both panels compare our values of T_{eff} and $\log(g)$ measured from high-resolution spectra against representative isochrones, with older stars in the left panel and younger stars in the right panel, and the majority of stars lie near the giant branch corresponding to the appropriate initial values. The horizontal lines in each panel mark the $\log(g)$ at the RGB bump for each isochrone shown, calculated from our empirical calibration given in Section 2.2. The squares represent stars that have not yet begun to ascend the RGB, and their high Li abundances are presumably primordial. The triangles represent RGB stars, both young and old, and the circles show red clump stars, which all sit to the left of the isochrone at their metallicity, and are all at intermediate age. The three crosses at the top of the left panel are three low-metallicity stars with parameters that are apparently inconsistent with the isochrones; we will address these stars in Sec. 5. The last two columns of Table 2 give our final estimates for age and evolutionary phase. These values are not given for the three stars with parameters incompatible with the isochrones.

We are able to determine $^{12}\text{C}/^{13}\text{C}$ for all six of our red clump stars, using synthesis of the 4297Å CH feature. In all of these stars, the ratio is fairly low ($^{12}\text{C}/^{13}\text{C} \leq 15$), indicating that first dredge-up has efficiently mixed the surface material with the stellar interior.

The Li-rich stars are mainly found low on the RGB, which might be expected from Li production associated with the onset of deep mixing. However, the presence of some bright Li-rich giants and red clump stars indicates that it must also be possible for a star to produce Li during other evolutionary phases. Current models of thermohaline mixing on the red giant branch are fairly unconstrained in terms of whether matter is transported away from the hydrogen-burning shell quickly enough for the Cameron-Fowler

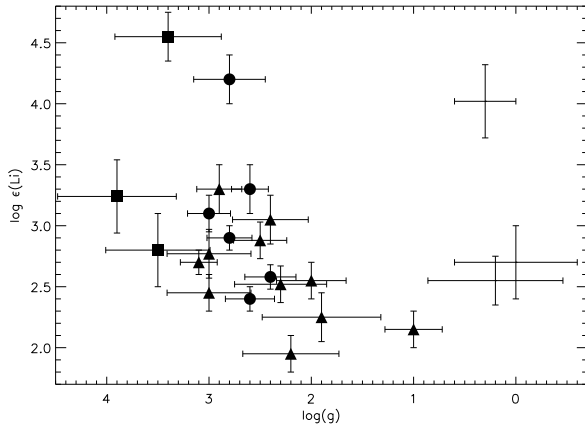


Figure 7. Lithium abundance versus surface gravity for the stars in our sample. The typical value for $\log \epsilon(\text{Li})$ decreases in the more evolved stars. Symbols are as in Figure 6, and there is no clear difference in the behavior of RGB stars and red clump stars in this plane.

mechanism to produce Li. Figures 7 and 8 show our resulting Li abundances versus $\log(g)$ and $[\text{Fe}/\text{H}]$, respectively, using the same symbols as in Figure 6.

5 DISCUSSION

We have identified 23 new Li-rich post-main-sequence stars: 5 bright red giants, 6 red clump stars, 6 RGB-bump stars, 3 lower-RGB stars and 3 post-AGB stars. Although schematic models exist for the production of Li at onset of deep mixing, near the RGB bump, there is not a clear theoretical explanation for the processes that produce and destroy Li in post-main-sequence stars.

There are no targets in common between our data set and the six recent studies mentioned in the Introduction. However, our initial search of the DR7 CAS included SEGUE observations in Galactic globular and open clusters, allowing a possible overlap with the studies of Pilachowski (1986) and Pilachowski et al. (1988). Our star SDSS J2356+5633 is the known Li-rich giant NGC 7789 K301 (Pilachowski 1986). It is chosen as a likely followup candidate according to our low-resolution selection criteria, and our high-resolution analysis confirms its high Li abundance. The fact that this star is in a cluster can be used to check our analysis. The mean metallicity of NGC 7789 is -0.04 ± 0.05 and 0.04 ± 0.07 from Tautvaišienė et al. (2005) and Pancino et al. (2010), respectively, which is consistent with our value of -0.05 ± 0.07 . In addition, for this star Pilachowski (1986) note that it is a weak G-band star, and we find that this star has one of the lowest carbon abundance ratios in our sample, $[\text{C}/\text{Fe}] = -0.7$. Further, the position of K301 on the CMD of NGC 7789 suggests that it may be an AGB star, or its low carbon abundance may cause the star to move blueward in the CMD via the Bond-Neff Effect (Bond & Neff 1969).

We do not recover the Li-rich stars discussed in Roederer et al. (2008), Kumar & Reddy (2009), Carney et al. (1998), Kraft et al. (1999), Smith et al. (1999) or Charbonnel & Balachandran (2000), which were not observed by SEGUE. Two of the Li-rich stars we selected for high-resolution followup are serendipitously located in the Kepler field. SDSS J1901+3808 is KIC 2968828, which has asteroseismology-based stellar parameters of $\log(g) = 2.393$, $T_{\text{eff}} = 4270$, $[\text{Fe}/\text{H}] = -0.823$. While the surface gravity is a good match to our determination, the temperature and metallicity are

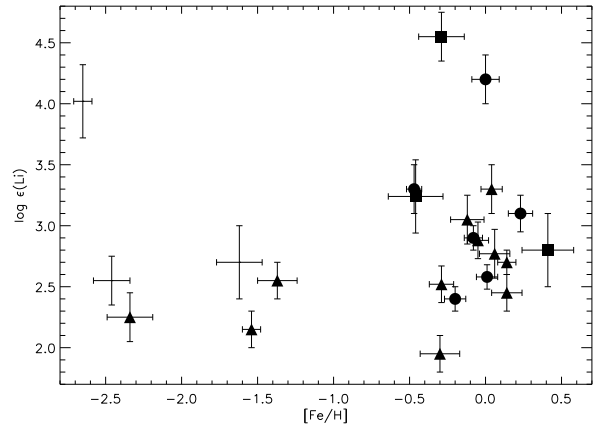


Figure 8. Lithium abundance versus metallicity for the stars in our sample. The higher-metallicity stars show a broader range in $\log \epsilon(\text{Li})$, and a higher mean, than the lower-metallicity stars. The rate of deep mixing is a sensitive function of stellar metallicity, so this may indicate that higher-metallicity stars are better able to produce lithium, or less able to destroy it. Symbols are as in Figure 6.

quite different, and we believe that the discrepancy is likely due to uncertainties in the Kepler analysis techniques. SDSS J1909+3837 is KIC 3531579, which does not have any publicly available Kepler data yet.

The three stars in our high-resolution data set that have stellar parameters incompatible with the isochrones are quite unusual. With their very low surface gravities, we identify them as post-AGB stars. The metallicities we derive for two of them are quite low ($[\text{Fe}/\text{H}] \sim -2.5$). With these very low metallicities, these two stars are marginally consistent with being RGB-tip stars, but the extremely low gravities are also consistent with a known population of metal-deficient post-AGB stars (Parthasarathy 2000). We note that it has been hypothesized that very low metallicities in post-AGB stars are a result of dust formation in extremely cool atmospheres and are not representative of the initial stellar composition.

5.1 Internal and external sources of lithium

The initial photometric association of Li-rich stars with the RGB bump and the red clump led naturally to a suggestion (Charbonnel & Balachandran 2000) that the destruction of the μ -barrier created by first dredge-up causes a brief episode of Li production. This cannot be the explanation for high Li abundances in bright giants, far from the RGB bump, but any process that causes rapid mass motion between the envelope and the hydrogen-burning shell could in principle produce Li at the surface via the Cameron-Fowler mechanism: ${}^3\text{He}(\alpha, \gamma){}^7\text{Be}(e^-, \nu){}^7\text{Li}$.

One potential mechanism for such stirring is proposed by Denissenkov (2012), who note that, in their models of red giants with rapid interior rotation, the temperature gradient in the region between the hydrogen-burning shell and the envelope can become quite large, permitting deep mixing to operate much more quickly than usual. One consequence of this accelerated deep mixing is that the photometric loop executed during the RGB bump is much more extended, pushing RGB-bump stars into the same color-magnitude region as red clump stars. This indicates that perhaps the Li-rich stars that have been identified as red clump stars (including the six in this study) are actually RGB-bump stars with rapid internal ro-

Table 2. ID and stellar parameters from high-resolution analysis, for the 23 stars for which we could determine high-resolution stellar parameters

SDSS ID	T_{eff}	σ	$\log(g)$	σ	[Fe/H]	σ	$v_{\text{turb}}(\text{kms}^{-1})$	σ	$v_{\text{rot}}(\text{kms}^{-1})$	Age (Gyr)	EP
SDSS J2206+4531	4700	159	3.5	0.51	+0.41	0.17	1.95	0.29	...	9	SGB
SDSS J2353+5728	5025	76	3.0	0.21	+0.23	0.08	1.67	0.11	...	4	RC
SDSS J0808-0815	4900	103	3.0	0.41	+0.14	0.10	1.72	0.14	...	2	RGB
SDSS J0301+7159	5075	63	3.1	0.18	+0.14	0.06	1.79	0.08	...	1	RC
SDSS J2019+6012	4800	100	3.0	0.41	+0.06	0.10	1.70	0.13	...	3	RGB
SDSS J0652+4052	4900	62	2.9	0.22	+0.04	0.07	1.73	0.08	...	2	RC
SDSS J0245+7102	4850	70	2.4	0.25	+0.01	0.07	1.77	0.07	...	4	RC
SDSS J0632+2604	5050	84	2.8	0.35	+0.00	0.09	1.84	0.11	...	4	RC
SDSS J2356+5633	4750	73	2.5	0.26	-0.05	0.07	2.00	0.07	...	1	RGB
SDSS J0535+0514	5200	64	2.8	0.22	-0.08	0.06	1.66	0.08	...	4	RC
SDSS J2200+4559	4675	100	2.4	0.37	-0.12	0.11	1.99	0.39	6	2	RGB
SDSS J0304+3823	5125	64	2.6	0.24	-0.20	0.07	1.33	0.09	...	4	RC
SDSS J1901+3808	4450	86	2.3	0.45	-0.29	0.08	1.78	0.09	...	4	RGB
SDSS J0720+3036	5250	142	3.4	0.52	-0.29	0.15	1.40	0.25	10	4	SGB
SDSS J1909+3837	4450	123	2.2	0.47	-0.30	0.13	2.13	0.13	...	4	RGB
SDSS J1105+2850	5625	156	3.9	0.58	-0.46	0.18	1.05	0.31	...	4	SGB
SDSS J0654+4200	5200	50	2.6	0.18	-0.47	0.05	1.88	0.06	12.5	4	RC
SDSS J1607+0447	5175	100	2.0	0.34	-1.37	0.13	1.49	0.15	...	10	RGB
SDSS J1310-0012	4550	66	1.0	0.28	-1.54	0.06	1.74	0.07	...	12	RGB
SDSS J0936+2935	5125	120	0.0	0.60	-1.62	0.15	2.59	0.23
SDSS J1522+0655	4975	140	1.9	0.58	-2.34	0.15	1.89	0.18	...	12	RGB
SDSS J0831+5402	4725	106	0.2	0.66	-2.46	0.12	2.32	0.23
SDSS J1432+0814	4625	38	0.3	0.3	-2.65	0.06	1.90	0.13	9.1

Table 3. ID and abundances from high-resolution analysis, for the 23 stars for which we could determine high-resolution stellar parameters

SDSS ID	$[\alpha/\text{Fe}]$	σ	$[\text{C}/\text{Fe}]$	σ	$^{12}\text{C}/^{13}\text{C}$	$\log\epsilon(\text{Li})_{6708}$	σ	$\log\epsilon(\text{Li})_{6104}$	σ
SDSS J2206+4531	-0.29	0.07	-0.5	0.3	...	2.80	0.30	≤ 2.9	...
SDSS J2353+5728	-0.08	0.06	-0.5	0.2	8	3.10	0.15	≤ 3.2	...
SDSS J0808-0815	-0.34	0.18	-0.6	0.2	...	2.45	0.15	≤ 2.7	...
SDSS J0301+7159	-0.15	0.08	-0.6	0.1	15	2.70	0.10	≤ 2.9	...
SDSS J2019+6012	-0.08	0.06	-0.7	0.2	...	2.77	0.20	≤ 2.8	...
SDSS J0652+4052	-0.05	0.06	-0.4	0.2	15	3.30	0.20	3.0	0.3
SDSS J0245+7102	-0.07	0.04	-0.4	0.1	15	2.58	0.10	2.4	0.4
SDSS J0632+2604	-0.08	0.05	-0.4	0.1	...	4.20	0.2	4.1	0.2
SDSS J2356+5633	+0.06	0.05	-0.7	0.1	...	2.88	0.15	2.9	0.2
SDSS J0535+0514	+0.06	0.04	-0.5	0.2	15	2.90	0.10	2.7	0.3
SDSS J2200+4559	+0.05	0.08	-0.8	0.2	...	3.05	0.20	3.0	0.2
SDSS J0304+3823	-0.01	0.04	-0.3	0.2	...	2.40	0.10	≤ 2.6	...
SDSS J1901+3808	+0.17	0.07	-0.7	0.1	...	2.52	0.15	2.4	0.3
SDSS J0720+3036	-0.23	0.13	-0.4	0.2	...	4.55	0.20	4.2	0.2
SDSS J1909+3837	-0.20	0.07	≤ -0.4	1.95	0.15	≤ 2.2	...
SDSS J1105+2850	+0.09	0.48	-0.4	0.4	...	3.24	0.30	≤ 2.9	...
SDSS J0654+4200	+0.02	0.06	-0.4	0.1	4	3.30	0.20	3.1	0.3
SDSS J1607+0447	+0.33	0.06	-0.6	0.2	...	2.55	0.15	2.7	0.3
SDSS J1310-0012	+0.32	0.09	-0.7	0.2	...	2.15	0.15	2.2	0.3
SDSS J0936+2935	+0.38	0.11	0.3	0.4	...	2.70	0.30	≤ 3.0	...
SDSS J1522+0655	+0.50	0.20	-0.7	0.3	...	2.25	0.20	2.6	0.4
SDSS J0831+5402	+0.33	0.11	0.1	0.3	...	2.55	0.20	≤ 2.7	...
SDSS J1432+0814	+0.12	0.10	-0.2	0.2	...	4.02	0.30	3.6	0.3

tation. Asteroseismic data on these stars could clarify their evolutionary phase. This process is an interesting possibility, but does not explain Li-rich bright RGB stars.

The engulfment of a giant planet has also been suggested (Carlberg et al. 2012) as a way to “replenish” the surface Li abundance of a red giant. This process should be distinguishable from intrinsic Li production by deep mixing, since the $^{12}\text{C}/^{13}\text{C}$ ratio should rise following planet accretion, but should fall as a result of

deep mixing. This is a process that could in principle happen at any point in stellar evolution, though the dramatic radial expansion that occurs as a star ascends the RGB would make it far more likely to happen during that phase.

6 SUMMARY

The work presented here demonstrates the potential of large spectroscopic surveys such as SEGUE as a source of unusual targets for followup observations. The ability to select our initial data set from a very broad parameter space allows us to search for Li-rich stars in a relatively unbiased way. Other followup studies based on SEGUE data (e.g., Caffau et al. 2011; Bonifacio et al. 2011; Aoki et al. 2012) follow the same approach: an initial search in a large, multidimensional parameter space, which introduces some heterogeneity in the data set, but can avoid biases inherent in more focused studies.

Although we agree with Kirby et al. (2012) that Li-rich field giants are perfectly normal stars in most respects, we must disagree with their conclusion, originally expressed by de La Reza et al. (1996), that the onset of deep mixing produces a brief phase of Li enrichment in all stars. Such a universal process would imply that Li-rich stars should only be found near the RGB bump, which they are not. We propose instead that deep mixing is capable of producing Li enrichment at any point above the RGB bump, based on thermohaline mixing models. This does not explain what triggers a phase of Li production, but does fit comfortably with the wide range of evolutionary phase that Li-rich stars occupy, and the short duration of the phase, which is inferred from the rarity of these stars.

The combination of the recent large-sample studies of Li-rich stars is extremely important for advancing our understanding of the origins of these stars. Primarily, the new data demonstrates the ubiquity of Li-rich stars across Galactic and extragalactic environments - Li production is clearly a stochastic and short-lived, possibly recurrent event in stellar evolution. The next significant step will need to take an approach similar to the study by Carlberg et al. (2012): identifying unique features of the various proposed sources for Li enrichment in post-main-sequence stars, such as correlated variations in particular elemental or isotopic abundances, and searching specifically for those signals.

REFERENCES

- Abazajian, K., Adelman-McCarthy, J. K., Agüeros, M. A., et al. 2004, *AJ*, 128, 502
- Abazajian, K., Adelman-McCarthy, J. K., Agüeros, M. A., et al. 2005, *AJ*, 129, 1755
- Abazajian, K., Adelman-McCarthy, J. K., Agüeros, M. A., et al. 2003, *AJ*, 126, 2081
- Abazajian, K. N., Adelman-McCarthy, J. K., Agüeros, M. A., et al. 2009, *ApJS*, 182, 543
- Adelman-McCarthy, J. K., Agüeros, M. A., Allam, S. S., et al. 2008, *ApJS*, 175, 297
- Adelman-McCarthy, J. K., Agüeros, M. A., Allam, S. S., et al. 2007, *ApJS*, 172, 634
- Adelman-McCarthy, J. K., Agüeros, M. A., Allam, S. S., et al. 2006, *ApJS*, 162, 38
- Aihara, H., Allende Prieto, C., An, D., et al. 2011, *ApJS*, 193, 29
- Allende Prieto, C., Sivarani, T., Beers, T. C., et al. 2008, *AJ*, 136, 2070
- Angelou, G. C., Church, R. P., Stancliffe, R. J., Lattanzio, J. C., & Smith, G. H. 2011, *ApJ*, 728, 79
- Aoki, W., Beers, T. C., Lee, Y. S., et al. 2012, *ArXiv e-prints*
- Bond, H. E. & Neff, J. S. 1969, *ApJ*, 158, 1235
- Bonifacio, P., Caffau, E., François, P., et al. 2011, *Astronomische Nachrichten*, 332, 251
- Brown, J. A., Sneden, C., Lambert, D. L., & Dutchover, Jr., E. 1989, *ApJS*, 71, 293
- Caffau, E., Bonifacio, P., François, P., et al. 2011, *Nature*, 477, 67
- Cameron, A. G. W. & Fowler, W. A. 1971, *ApJ*, 164, 111
- Carlberg, J. K., Cunha, K., Smith, V. V., & Majewski, S. R. 2012, *ApJ*, 757, 109
- Carney, B. W., Fry, A. M., & Gonzalez, G. 1998, *AJ*, 116, 2984
- Charbonnel, C. & Balachandran, S. C. 2000, *A&A*, 359, 563
- de La Reza, R., Drake, N. A., & da Silva, L. 1996, *ApJL*, 456, L115
- Demarque, P., Woo, J.-H., Kim, Y.-C., & Yi, S. K. 2004, *ApJS*, 155, 667
- Denissenkov, P. A. 2012, *ApJL*, 753, L3
- Frebel, A., Roederer, I. U., Shetrone, M., et al. 2008, in *Astronomical Society of the Pacific Conference Series*, Vol. 393, New Horizons in Astronomy, ed. A. Frebel, J. R. Maund, J. Shen, & M. H. Siegel, 207
- Fukugita, M., Ichikawa, T., Gunn, J. E., et al. 1996, *AJ*, 111, 1748
- Fulbright, J. P., McWilliam, A., & Rich, R. M. 2006, *ApJ*, 636, 821
- Fulbright, J. P., McWilliam, A., & Rich, R. M. 2007, *ApJ*, 661, 1152
- Fusi Pecci, F., Ferraro, F. R., Crocker, D. A., Rood, R. T., & Buonanno, R. 1990, *A&A*, 238, 95
- Ge, J., Mahadevan, S., Lee, B., et al. 2008, in *Astronomical Society of the Pacific Conference Series*, Vol. 398, Extreme Solar Systems, ed. D. Fischer, F. A. Rasio, S. E. Thorsett, & A. Wolsczhan, 449
- Gonzalez, O. A., Zoccali, M., Monaco, L., et al. 2009, *A&A*, 508, 289
- Gunn, J. E., Carr, M., Rockosi, C., et al. 1998, *AJ*, 116, 3040
- Gunn, J. E., Siegmund, W. A., Mannery, E. J., et al. 2006, *AJ*, 131, 2332
- Gustafsson, B., Edvardsson, B., Eriksson, K., et al. 2008, *A&A*, 486, 951
- Iben, I. J. 1968, *ApJ*, 154, 581
- Johnson, C. I. & Pilachowski, C. A. 2010, *ApJ*, 722, 1373
- Kirby, E. N., Cohen, J. G., Smith, G. H., et al. 2011, *ApJ*, 727, 79
- Kirby, E. N., Fu, X., Guhathakurta, P., & Deng, L. 2012, *ApJL*, 752, L16
- Koch, A., Grebel, E. K., Gilmore, G. F., et al. 2008, *AJ*, 135, 1580
- Koch, A. & McWilliam, A. 2008, *AJ*, 135, 1551
- Kraft, R. P., Peterson, R. C., Guhathakurta, P., et al. 1999, *ApJL*, 518, L53
- Kumar, Y. B. & Reddy, B. E. 2009, *ApJL*, 703, L46
- Kumar, Y. B., Reddy, B. E., & Lambert, D. L. 2011, *ApJL*, 730, L12
- Kurucz, R. & Bell, B. 1995, *Atomic Line Data* (R.L. Kurucz and B. Bell) Kurucz CD-ROM No. 23. Cambridge, Mass.: Smithsonian Astrophysical Observatory, 1995., 23
- Lebzelter, T., Uttenthaler, S., Busso, M., Schultheis, M., & Aringer, B. 2012, *A&A*, 538, A36
- Lee, Y. S., Beers, T. C., Sivarani, T., et al. 2008a, *AJ*, 136, 2022
- Lee, Y. S., Beers, T. C., Sivarani, T., et al. 2008b, *AJ*, 136, 2050
- Martell, S. L., Smith, G. H., & Briley, M. M. 2008, *AJ*, 136, 2522
- Monaco, L., Villanova, S., Moni Bidin, C., et al. 2011, *A&A*, 529, A90
- Pancino, E., Carrera, R., Rossetti, E., & Gallart, C. 2010, *A&A*, 511, A56
- Parthasarathy, M. 2000, in *IAU Symposium*, Vol. 177, The Carbon Star Phenomenon, ed. R. F. Wing, 225
- Pier, J. R., Munn, J. A., Hindsley, R. B., et al. 2003, *AJ*, 125, 1559

Pilachowski, C. 1986, *ApJ*, 300, 289
 Pilachowski, C., Saha, A., & Hobbs, L. M. 1988, *PASP*, 100, 474
 Pilachowski, C. A., Sneden, C., Kraft, R. P., Harmer, D., & Willmarth, D. 2000, *AJ*, 119, 2895
 Roederer, I. U., Frebel, A., Shetrone, M. D., et al. 2008, *ApJ*, 679, 1549
 Ruchti, G. R., Fulbright, J. P., Wyse, R. F. G., et al. 2011, *ApJ*, 743, 107
 SDSS-III Collaboration, :, Ahn, C. P., et al. 2012, *ArXiv e-prints*
 Shetrone, M., Cornell, M. E., Fowler, J. R., et al. 2007, *PASP*, 119, 556
 Shetrone, M., Venn, K. A., Tolstoy, E., et al. 2003, *AJ*, 125, 684
 Smith, G. H. 2002, *PASP*, 114, 1097
 Smith, V. V., Shetrone, M. D., & Keane, M. J. 1999, *ApJL*, 516, L73
 Smolinski, J. P., Lee, Y. S., Beers, T. C., et al. 2011, *AJ*, 141, 89
 Sneden, C. A. 1973, PhD thesis, THE UNIVERSITY OF TEXAS AT AUSTIN.
 Stoughton, C., Lupton, R. H., Bernardi, M., et al. 2002, *AJ*, 123, 485
 Tautvaišienė, G., Edvardsson, B., Puzeras, E., & Ilyin, I. 2005, *A&A*, 431, 933
 Tull, R. G. 1998, in *Society of Photo-Optical Instrumentation Engineers (SPIE) Conference Series*, Vol. 3355, *Society of Photo-Optical Instrumentation Engineers (SPIE) Conference Series*, ed. S. D’Odorico, 387–398
 Venn, K. A., Kaufer, A., Tolstoy, E., et al. 2003, in *IAU Symposium*, Vol. 212, *A Massive Star Odyssey: From Main Sequence to Supernova*, ed. K. van der Hucht, A. Herrero, & C. Esteban, 30
 Wallerstein, G. & Sneden, C. 1982, *ApJ*, 255, 577
 Yanny, B., Rockosi, C., Newberg, H. J., et al. 2009, *AJ*, 137, 4377
 York, D. G., Adelman, J., Anderson, Jr., J. E., et al. 2000, *AJ*, 120, 1579

University, New York University, Ohio State University, Pennsylvania State University, University of Portsmouth, Princeton University, the Spanish Participation Group, University of Tokyo, University of Utah, Vanderbilt University, University of Virginia, University of Washington, and Yale University.

This research has made use of the VizieR catalogue access tool, CDS, Strasbourg, France. The original description of the VizieR service was published in *A&AS* 143, 23.

ACKNOWLEDGEMENTS

We appreciate thoughtful comments from an anonymous referee, which have made this paper clearer.

During this work, SLM was supported by Sonderforschungsbereich SFB 881 “The Milky Way System” (subprojects A2 and A5) of the German Research Foundation (DFG).

The Hobby-Eberly Telescope (HET) is a joint project of the University of Texas at Austin, the Pennsylvania State University, Ludwig-Maximilians-Universität München, and Georg-August-Universität Göttingen. The HET is named in honor of its principal benefactors, William P. Hobby and Robert E. Eberly.

Funding for SDSS-III has been provided by the Alfred P. Sloan Foundation, the Participating Institutions, the National Science Foundation, and the U.S. Department of Energy. The SDSS-III web site is <http://www.sdss3.org/>.

SDSS-III is managed by the Astrophysical Research Consortium for the Participating Institutions of the SDSS-III Collaboration including the University of Arizona, the Brazilian Participation Group, Brookhaven National Laboratory, University of Cambridge, University of Florida, the French Participation Group, the German Participation Group, the Instituto de Astrofísica de Canarias, the Michigan State/Notre Dame/JINA Participation Group, Johns Hopkins University, Lawrence Berkeley National Laboratory, Max Planck Institute for Astrophysics, New Mexico State

APPENDIX A: COMPARISON OF HIGH-RESOLUTION AND SSPP STELLAR PARAMETERS

During the course of this project, revised SSPP stellar parameters (including effective temperature, surface gravity and metallicity) were published for our stars as part of SDSS Data Release 9 (SDSS-III Collaboration et al. 2012). Since we have derived atmospheric parameters from our high-resolution spectra, we present here a brief study of the comparison between the DR9 SSPP and high-resolution parameters, for the 20 stars with reasonable high-resolution parameters. High-resolution stellar parameters are listed in Table 2; DR9 SSPP parameters for the same stars are given in Table A1.

Figures A1, A2 and A3 compare the high-resolution values for T_{eff} , $\log(g)$ and $[\text{Fe}/\text{H}]$, respectively, to the DR9 SSPP values, for the 20 stars with reasonable high-resolution parameters. There is scatter, but not a significant trend, between the high-resolution and SSPP determinations of T_{eff} and $[\text{Fe}/\text{H}]$, but we find a significant trend with little scatter between high-resolution and SSPP determinations of $\log(g)$. We also find a significant trend, with a slope of 102 ± 39 K/dex, between $T_{eff}^{\text{HRS}} - T_{eff}^{\text{SSPP}}$ and $[\text{Fe}/\text{H}]^{\text{SSPP}}$, indicating that the SSPP algorithms are somewhat susceptible to temperature-metallicity degeneracy. The fact that we use different iron lines to determine $[\text{Fe}/\text{H}]$ for the metal-poor and metal-rich stars in our sample could also contribute to this trend, but we would not expect that to cause an effect as large as what is observed.

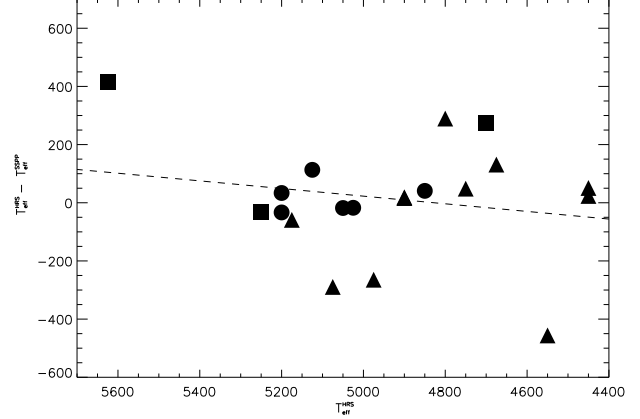


Figure A1. Difference between high-resolution and DR9 SSPP determinations of T_{eff} , as a function of high-resolution T_{eff} . The best-fit dashed line is consistent with no offset between the two temperature scales, but significant scatter. Symbols are as in Figure 6.

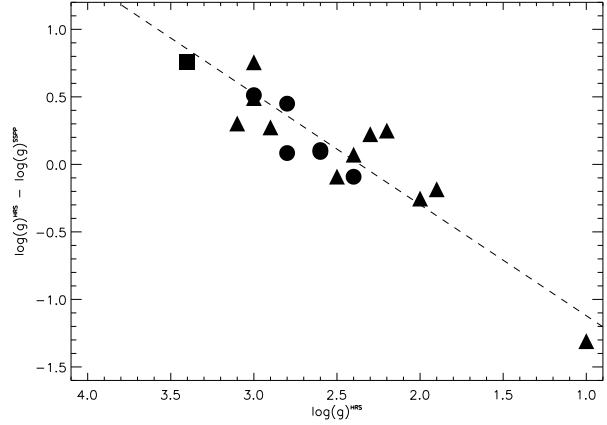
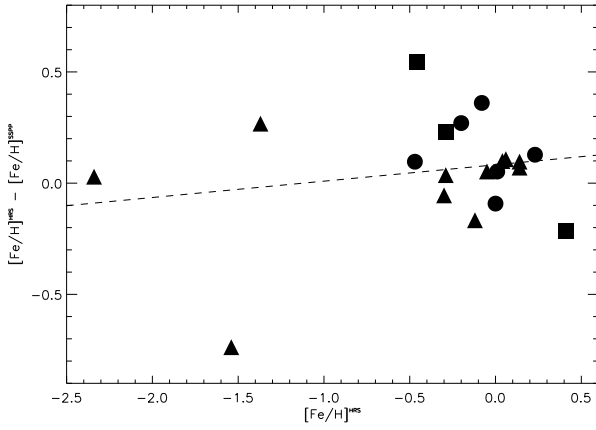


Figure A2. Difference between high-resolution and DR9 SSPP determinations of $\log(g)$, as a function of high-resolution $\log(g)$. The best-fit dashed line shows a significant trend. The SSPP is known to have difficulty determining $\log(g)$ in low-gravity stars, since the indicators it uses lose sensitivity; however, the trend to high gravity is unexpected. Symbols are as in Figure 6.

Table A1. ID and stellar parameters from the DR9 SSPP, for the 23 stars for which we could determine high-resolution stellar parameters

SDSS ID	T_{eff}	σ	$\log(g)$	σ	$[\text{Fe}/\text{H}]$	σ
SDSS J2206+4531	4426	15	2.23	0.08	0.62	0.007
SDSS J2353+5728	5042	88	2.49	0.09	0.10	0.036
SDSS J0808-0815	4884	9	2.51	0.15	0.04	0.009
SDSS J0301+7159	5364	147	2.80	0.14	0.07	0.05
SDSS J2019+6012	4510	70	2.24	0.13	-0.05	0.008
SDSS J0652+4052	4881	88	2.63	0.16	-0.06	0.043
SDSS J0245+7102	4809	113	2.49	0.21	-0.04	0.034
SDSS J0632+2604	5068	25	2.72	0.22	0.09	0.074
SDSS J2356+5633	4702	72	2.59	0.32	-0.10	0.009
SDSS J0535+0514	5166	47	2.35	0.18	-0.44	0.058
SDSS J2200+4559	4544	41	2.33	0.12	0.05	0.003
SDSS J0304+3823	5012	30	2.49	0.14	-0.47	0.031
SDSS J1901+3808	4399	88	2.08	0.08	-0.33	0.014
SDSS J0720+3036	5281	79	2.65	0.10	-0.52	0.036
SDSS J1909+3837	4426	110	1.95	0.31	-0.25	0.073
SDSS J1105+2850	5210	56	2.63	0.10	-1.00	0.026
SDSS J0654+4200	5233	20	2.51	0.06	-0.57	0.031
SDSS J1607+0447	5234	56	2.25	0.14	-1.64	0.045
SDSS J1310-0012	5006	244	2.31	0.20	-0.80	0.062
SDSS J0936+2935	5334	35	2.03	0.07	-1.28	0.058
SDSS J1522+0655	5240	46	2.08	0.20	-2.37	0.034
SDSS J0831+5402	4826	80	0.79	0.31	-2.66	0.053
SDSS J1432+0814	4664	239	1.43	0.29	-3.14	0.072

**Figure A3.** Difference between high-resolution and DR9 SSPP determinations of $[\text{Fe}/\text{H}]$, as a function of high-resolution $[\text{Fe}/\text{H}]$. A best-fit line is shown; however, this distribution is consistent with a small offset between the two metallicity scales and $\simeq 0.3$ dex scatter. Symbols are as in Figure 6.